

Non-Hermitian Chiral Skin Effect

Xin-Ran Ma,^{1,*} Kui Cao,^{1,*} Xiao-Ran Wang,² Zheng Wei,¹ Qian Du,¹ and Su-Peng Kou^{1,†}

¹*Center for Advanced Quantum Studies, Department of Physics,
Beijing Normal University, Beijing 100875, China*

²*College of Teacher Education, Hebei Normal University, Shijiazhuang 050024, China*

The interplay between non-Hermitian effects and topological insulators has become a frontier of research in non-Hermitian physics. However, the existence of a non-Hermitian skin effect for topological-protected edge states remains controversial. In this paper, we discover an alternative form of the non-Hermitian skin effect called the non-Hermitian chiral skin effect (NHCSE). NHCSE is a non-Hermitian skin effect under periodic boundary condition rather than open boundary condition. Specifically, the chiral modes of the NHCSE localize around “topological defects” characterized by global dissipation rather than being confined to the system boundaries. We show its detailed physical properties by taking the non-Hermitian Haldane model as an example. As a result, the intrinsic mechanism of the hybrid skin-topological effect in Chern insulators is fully understood via NHCSE. Therefore, this progress will be helpful for solving the controversial topic of hybrid skin-topological effect and thus benefit the research on both non-Hermitian physics and topological quantum states.

I. INTRODUCTION

The non-Hermitian quantum systems have attracted intensive attention due to their effectiveness in describing non-equilibrium and open systems, as well as their rich underlying physics distinguishing them from Hermitian counterparts[1–10]. There are many intriguing phenomena in non-Hermitian quantum systems, such as exceptional degeneracies[1, 11], unidirectional transmission[12, 13] and non-Hermitian skin effect (NHSE) [14–39]. The NHSE has the eigenstates of the bulk that are exponentially localized at the edge of the system with an open boundary condition (OBC) and can be characterized by the generalized Brillouin zone (GBZ) rather than the usual Brillouin zone (BZ) [18–20, 40]. In addition, the NHSE is pointed out to be relevant to point-gap topology and be identified by a corresponding “*winding number*”[26, 41]. The existence of the “*winding number*” guarantees the NHSE.

The investigation of the interplay between the NHSE and topological insulators has yielded a plethora of captivating physical phenomena. These include the emergence of defective edge states [42, 43], the development of non-Hermitian topological invariants [17, 18, 21, 26, 44], as well as the manifestation of synergy and hybridization between the NHSE and band topology in higher dimensions [4, 37, 38, 45–53]. Specifically, the hybrid skin-topological effect, which represents a distinct manifestation of NHSE, manifests exclusively in topological edge states and is confined to systems of two and higher dimensions. This effect results in the localization of topologically protected edge states at specific corners while the bulk states are extended. Previous investigations have found two types of the hybrid skin-topological effect: those induced by non-reciprocal lattice configurations [38, 50, 54] and those induced by gain and loss [37].

Notably, an important observation has been documented in a two-dimensional Chern insulator, where chiral edge states are localized at certain corners due to gain/loss [37]. This observation holds significant implications as chiral states exhibit robustness against backscattering and Anderson localization in Hermitian systems. Nevertheless, a comprehensive understanding of the underlying mechanisms governing the gain-loss-induced hybrid skin-topological effect remains challenging.

In this paper, we try to solve this puzzle after answering the following questions: (i) Is there a fundamental distinction between the NHSE that occurs in bulk states and that appears in topological edge states of a Chern insulator? (ii) If such a distinction exists, how can we determine whether NHSE occurs in topological edge states, and how to characterize it? (iii) What is the physical basis for these distinctions, and how do they relate to the hybrid skin-topological effect? Can we have a deeper understanding of the hybrid skin-topological effect with the help of NHSE for topological edge states?

To answer the above questions, we investigate the non-Hermitian chiral skin effect (NHCSE) under periodic boundary conditions (PBC) by studying chiral modes with inhomogeneous, perturbative dissipation. Specifically, we analyze the non-Hermitian Haldane model and examine the influence of global dissipation’s domain walls (GDDWs) as a form of inhomogeneous dissipation. Our focus is on two key properties of NHSE: the anomalous occurrence exclusively of GDDWs in topological systems of two or higher dimensions, and the phenomenon of boundary reconstruction in cylindrical Chern insulators with GDDWs on one edge. Moreover, our study presents a novel mechanism for the hybrid skin-topological effect by introducing the concept of the NHCSE.

This work is organized as follows. Sec. II provides an introduction to the theory of the NHCSE. In Sec. III, we investigate the non-Hermitian Haldane model with inhomogeneous and perturbative dissipation. Specifically, we investigate the cases of bulk dissipation in Sec. IV and edge dissipation in Sec. V to explore the manifestation of the NHCSE. In Sec. VI, we use NHCSE to understand

*Who has the same contribution to this work

†Electronic address: spkou@bnu.edu.cn

the hybrid skin-topological effect. Moreover, in Sec. VII, we introduce a circuit design capable of implementing the NHCSE in the Haldane model with GDDWs. Finally, we conclude our work in Sec. VIII.

II. NON-HERMITIAN CHIRAL SKIN EFFECT

Firstly, we show the key properties of the NHCSE for chiral modes with inhomogeneous dissipation. We emphasize that NHCSE is a unique type of NHSE under PBC rather than OBC.

In the continuous limit, the effective single-body Hamiltonian for chiral modes in low-energy physics becomes

$$h_{\text{chiral}} = v \cdot k, \quad (1)$$

where v is the velocity of edge states, and k is the wave vector of the chiral modes. There are two types of chiral modes, one with positive velocity $v > 0$, the other with negative velocity $v < 0$. Then, we consider the effect of dissipation, of which the effective strength is γ ($\text{Im}\gamma \equiv 0$), and the effective Hamiltonian of chiral modes turns into

$$h_{\text{chiral}} = v \cdot k + i\gamma = v \cdot (k - ik_0), \quad (2)$$

where $k_0 = -\gamma/v$. There is a notable aspect of chiral modes that *dissipation plays the role of an imaginary wave vector*[42].

In general, chiral modes are realized as topologically protected edge states on the boundaries of a 2D Chern insulator. Therefore, topological edge states are chiral modes under PBC rather than OBC. *Does there exist NHSE for the chiral modes with PBC? The answer is Yes!*

To answer the above questions, we consider a non-Hermitian Hamiltonian for chiral states with inhomogeneous, perturbative dissipation $\gamma(x)$ ($x \in [0, L]$, $|\gamma(x)| \ll 1$). Additionally, we establish PBC as $\psi(0) = \psi(L)$. The wave functions in $x \in [0, L]$ is expressed as

$$\psi_k(x) = \frac{1}{\mathcal{N}} e^{ikx} e^{\frac{1}{v} \int_0^x [\gamma(x') - \bar{\gamma}] dx'}, \quad (3)$$

where \mathcal{N} is a normalized coefficient, k is the given wave number satisfying $k = (2\pi n)/L$ ($n \in \mathbb{Z}$), and $\bar{\gamma}$ is the average value of the integral of inhomogeneous dissipation in real space, given by

$$\bar{\gamma} = \frac{1}{L} \int_0^L \gamma(x) dx. \quad (4)$$

The energy levels for chiral modes become

$$E_{\text{chiral}} = v \cdot k + i\bar{\gamma}, \quad (5)$$

forming a straight line with fixed imaginary part $\bar{\gamma}$ in complex energy space. Eq. (3) and Eq. (5) are derived in Appendix A. Before discussing NHCSE, we introduce *global dissipation* and its topological defects — *global dissipation's domain wall* (GDDW).

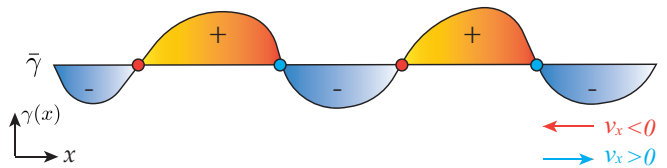


FIG. 1: The illustration of NHCSE for chiral modes with inhomogeneous dissipation in the continuous limit. The red regions represent $\gamma_{\text{global}}(x) > 0$, and the blue regions represent $\gamma_{\text{global}}(x) < 0$. The red arrow and blue arrow represent the direction of chiral current $v_x < 0, v_x > 0$, respectively. The chiral edge states ($v_x < 0$) localised at the A-type GDDWs x_0^+ (red dots), and the chiral edge states ($v_x > 0$) localised at the B-type GDDWs x_0^- (blue dots).

Definition 1: Global dissipation: Global dissipation is defined as $\gamma_{\text{global}}(x) = \gamma(x) - \bar{\gamma}$ where $\bar{\gamma}$ is the average value of inhomogeneous dissipation $\bar{\gamma} = \frac{1}{L} \int_0^L \gamma(x) dx$. The integral path is a closed loop along the boundary of the chiral edge state.

Definition 2: Global dissipation's domain walls: (1) If there exists x_0^+ that satisfies $\gamma_{\text{global}}(x_0^+ + 0^-) < 0$ and $\gamma_{\text{global}}(x_0^+ + 0^+) > 0$, we denote x_0^+ as an A-type GDDW. (2) If there exists x_0^- that satisfies $\gamma_{\text{global}}(x_0^- + 0^-) > 0$ and $\gamma_{\text{global}}(x_0^- + 0^+) < 0$, we denote x_0^- as a B-type GDDW.

As shown in Fig. 1, the A-type GDDWs represent red dots, and B-type GDDWs represent blue dots. To determine the positions x_0^\pm according to definitions 1 and 2, it is necessary to integrate the inhomogeneous dissipation over the closed loop along the boundary of the chiral edge state in order to obtain $\bar{\gamma}$. This is why we refer to it as the “global” dissipation’s domain wall. Furthermore, this highlights that the NHCSE is a type of NHSE specifically under PBC. Subsequently, we present the critical properties of the NHCSE.

Definition 3: The wave function is defined as localized at x_0^\pm within the interval $[a, b]$ if the squared modulus of the wave function is monotonically increasing in the interval $[a, x_0^\pm)$ and monotonically decreasing in the interval $(x_0^\pm, b]$ when $a < x_0^\pm < b$.

Theorem: If $\gamma_{\text{global}}(x)$ is a continuous function, then a chiral mode with the negative speed is localized at x_0^+ (within a certain interval) if and only if there exists an A-type GDDW at x_0^+ . Furthermore, a chiral mode with the positive speed is localized at x_0^- (within a certain interval) if and only if there exists a B-type GDDW at x_0^- .

We show detailed proofs and examples in Appendix B and C.

This result gives rise to an interesting effect, the NHCSE, signifying the existence of NHSE for chiral modes under PBC. In particular, NHCSE is quite different from the usual NHSE (or higher-order NHSE) for bulk states under OBC. For NHCSE, there *does not* exist point-like topology configuration in complex spectrum [26, 41]. Instead, in complex spectrum, the energy levels for chiral modes with NHCSE have a structure of a line rather than a closed loop. It is non-zero global dissipation

$\gamma_{\text{global}} = \gamma(x) - \bar{\gamma} \neq 0$ in real space rather than a certain “winding number” in complex spectrum that plays the role of an “order parameter” characterizing NHCSE. A zero effective dissipation γ_{global} indicates the vanishing of NHCSE. The bigger of γ_{global} , the stronger of NHCSE.

In the following parts, NHCSE is applied to the topologically protected edge states in 2D Chern insulators with inhomogeneous dissipation. With the help of this toy lattice model, an additional property of NHCSE — *anomaly* will be demonstrated.

III. MODEL

In this section, we consider chiral modes on the boundary of the non-Hermitian Haldane model with inhomogeneous, perturbative dissipation to describe the properties of NHCSE. The Haldane model is a typical (Hermitian) model of a 2D Chern insulator on a honeycomb lattice [56, 57], of which the Hamiltonian is

$$\hat{H}_{\text{haldane}} = t_1 \sum_{\langle ij \rangle} c_i^\dagger c_j + t_2 \sum_{\langle\langle ij \rangle\rangle} e^{i\phi_{ij}} c_i^\dagger c_j, \quad (6)$$

where c_i^\dagger and c_i are creation and annihilation operators for a particle at the i -th site. $\langle i, j \rangle$ and $\langle\langle i, j \rangle\rangle$ denote the nearest-neighbor (NN) hopping and the next-nearest-neighbor (NNN) hopping, and t_1 and t_2 are the strength of NN hopping and NNN hopping, respectively. $e^{i\phi_{ij}}$ is a complex phase of the NNN hopping, and we set the direction of the positive phase as clockwise ($|\phi_{ij}| = \frac{\pi}{2}$). In this paper, we set t_1 to be a unit, and t_2 to be constant, i.e., $t_2 \equiv 0.2t_1$.

The topological characterization of the Haldane model is captured by the Chern number Q . Due to the existence of nonzero Chern number $Q = 1$, there exist topological edge states propagating along the system’s edge [56]. For a system with PBC along x direction, and an OBC along y direction with zigzag edges, the effective (single-body) Hamiltonian of topological edge states $h_{\text{edge}}(k_x)$ becomes

$$h_{\text{edge}}(k_x) = \pm v_{\text{eff}} \cdot \sin k_x, \quad (7)$$

where v_{eff} characterizes the speed of topological edge states and can be described as [59]

$$v_{\text{eff}} = \frac{6t_1 t_2}{\sqrt{t_1^2 + 8t_2^2(1 - \cos k_x)}}. \quad (8)$$

According to $h_{\text{edge}}(k_x)$, we say that the topological edge states of such a Chern insulator on a honeycomb lattice are chiral modes.

To illustrate the NHCSE, we consider a non-Hermitian Haldane model with inhomogeneous, perturbative dissipation. The Hamiltonian becomes

$$\hat{H}_{\text{total}} = \hat{H}_{\text{haldane}} + \delta\hat{H}_{\text{D}}, \quad (9)$$

where $\delta\hat{H}_{\text{D}}$ represents the term associated with dissipation. In the subsequent sections, we investigate the

NHCSE for three cases of $\delta\hat{H}_{\text{D}}$: (a) Bulk dissipation (Section IV), (b) Dissipation on a single outermost zigzag edge (Section V), and (c) Staggered on-site gain/loss (Section VI).

IV. NON-HERMITIAN CHIRAL SKIN EFFECT FOR BULK DISSIPATION DWS

Now, we consider bulk’s dissipation on the Haldane model, i.e.,

$$\delta\hat{H}_{\text{D}} = i \sum_{\text{bulk}} \gamma_i c_i^\dagger c_i. \quad (10)$$

where γ_i represents the strength of dissipation at the i -th lattice site among all lattice sites. Firstly, we discuss the Haldane model with uniform bulk dissipation, $\gamma_i = \gamma$. When $\gamma \neq 0$, the imaginary part of energy levels $E(k_x, y)$ in complex spectrum have a global, uniform, shift,

$$\text{Im}E(k_x, y) = 0 \rightarrow \text{Im}E(k_x, y) \equiv \gamma. \quad (11)$$

The dispersion relations of both edge modes are given by

$$h_{\text{edge}}(k_x) = \pm v_{\text{eff}} \cdot \sin k_x + i\gamma. \quad (12)$$

In continuous limit, near $k_x = \pi$, $h_{\text{edge}}(k_x)$ is reduced into Eq. (2), i.e.,

$$h_{\text{edge}}(k_x) \simeq \pm v_{\text{eff}} \cdot (\Delta k \pm i\gamma/v_{\text{eff}}) \quad (13)$$

where $\Delta k = k_x - \pi$.

Next, to verify the existence of NHCSE, we discuss the Haldane model in the cylinder geometry (x PBC/ y OBC) with inhomogeneous bulk dissipation by considering a pair of GDDWs in bulk. As shown in Fig. 2(a) and (b), the cases where there is a difference in the bulk’s dissipation between the left and right regions are investigated. In both model, we show the existence of NHCSE — the energy levels of topological edge states become a line in the complex energy spectrum [Fig. 2(a) and (b)] and the topological edge states accumulate around the GDDWs [Fig. 2(c)]. In addition, the numerical results match our analytical prediction based on Eq. (12) [Fig. 2(d)]. The localization length ξ becomes

$$\xi = \frac{v_{\text{eff}}}{\gamma}, \quad (14)$$

and the specific derivations can be found in Appendix C.

In summary, such NHCSE can never be characterized by the certain point-like topology configuration in complex spectrum or corresponding “winding number”! Instead, it is global dissipation γ_{global} that can characterize the strength of NHCSE.

V. NON-HERMITIAN CHIRAL SKIN EFFECT FOR EDGE DISSIPATION DWS

We then consider the effect of inhomogeneous dissipation on the single outermost zigzag edge, i.e.,

$$\delta\hat{H}_{\text{D}} = i \sum_{\text{lower-edge}} \gamma_i c_i^\dagger c_i. \quad (15)$$

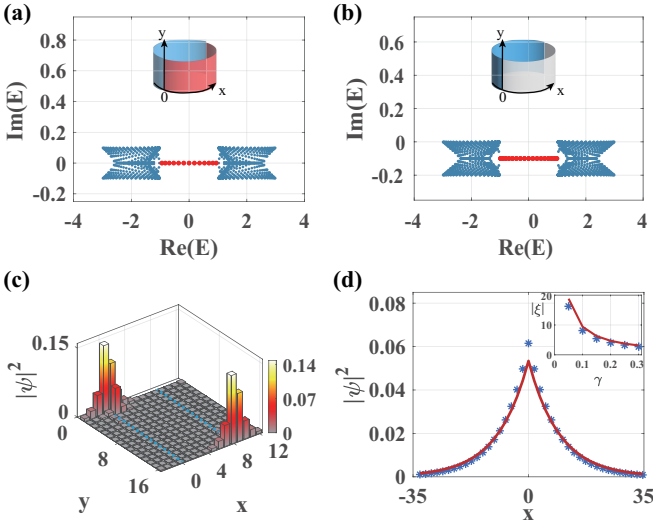


FIG. 2: Non-Hermitian Haldane model in the cylinder geometry (x PBC/ y OBC) with GDDWs in bulk. (a)-(b) The complex spectra with GDDWs (a) $\gamma_L = -0.1t_1, \gamma_R = 0.1t_1$ and (b) $\gamma_L = -0.2t_1, \gamma_R = 0$. The blue and red dots represent the energy levels of bulk states and topological edge states, respectively. (c) Particle distribution of the topological edge states. The dissipation is set as $\gamma_R(0 < x < 8) = 0.2t_1, \gamma_L(-4 < x < 0, 8 < x < 12) = -0.2t_1$. (d) Comparison between numerical results (blue stars) and theoretical predictions (red line) of the particle distribution of a topological edge state at the edge ($y = 0$). The inset displays the localization length ξ for varying strengths of γ . The numerical results are obtained from the Non-Hermitian Haldane model, while the theoretical results are derived from Eq. (14). Both wave functions are normalized along the x direction.

A. Effective Model for Topological Edge States: Half Hatano-Nelson model

First, we point out that *the effective model for topological edge states in this condition is Half Hatano-Nelson model that could exactly characterize NHCSE*. The effective Hamiltonian for the topological edge states is given by

$$h_{\text{edge}}(k_x) = \pm v_{\text{eff}} \cdot \sin k_x + i\gamma_{\text{eff}}, \quad (16)$$

where $k_x = \pi + \delta k$, and γ_{eff} represents the effective dissipation, defined as

$$\gamma_{\text{eff}} = \text{Im} \langle \psi_{\text{edge}} | \hat{H}_{\text{total}} | \psi_{\text{edge}} \rangle. \quad (17)$$

Here, ψ_{edge} denotes the wave functions of the chiral modes.

To accurately characterize NHCSE, we obtain the effective Hamiltonian for topological edge states by data fitting the effective dissipation for a uniform case $\gamma_i = \gamma$. Now, we have

$$\gamma_{\text{eff}}(k_x) = \sum_n a_n \cos nk_x. \quad (18)$$

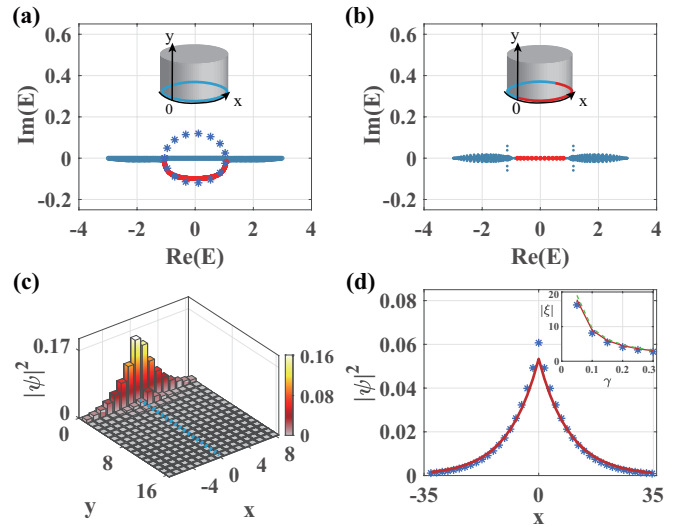


FIG. 3: Non-Hermitian Haldane model in the cylinder geometry (x PBC/ y OBC) with dissipation on a single outermost zigzag edge ($y = 0$). (a)-(b) Complex spectra with (a) uniform dissipation $\gamma = -0.1t_1$ and (b) GDDW ($\gamma_L = -0.1t_1, \gamma_R = 0.1t_1$). Blue dots, red dots, and cobalt blue stars represent energy levels of bulk states, topological edge states in the non-Hermitian Haldane model, and energy levels of effective 1D Hatano-Nelson model [Eq. (19)], respectively. (c) Particle distribution of topological edge states. The GDDW is set as $\gamma_R(x > 0) = 0.2t_1, \gamma_L(x < 0) = -0.2t_1$. (d) Comparison between numerical and theoretical results for the particle distribution of topological edge states at $y = 0$. The inset shows the localization length ξ for varying dissipation strengths γ . Blue stars, red lines, and green dash lines represent numerical results for the non-Hermitian Haldane model, theoretical results for the half Hatano-Nelson model [Eq. (21)], and continuous limits [Eq. (14)]. Both wave functions are normalized along the x direction.

For example, in the case of $\gamma = 0.1t_1$, we have $a_1 \simeq 0.12t_1, a_2 \simeq 0.023t_1$. As a result, the effective Hamiltonian for chiral edge states $\hat{h}_{\text{edge}}(\hat{k}_x)$ with uniform edge dissipation becomes half of a 1D Hatano-Nelson model described by

$$h_{\text{edge}}(k_x) = h_{\text{half-HN}}(k_x) \simeq v_{\text{eff}} \sin k_x + i\gamma_{\text{eff}}(k_x), \quad k_x \in (-\pi/2, \pi/2], \quad (19)$$

where $\gamma_{\text{eff}}(k_x) = a_1 \cos k_x + a_2 \cos 2k_x$. For clarity, we map Eq.(19) to the usual 1D generalized Hatano-Nelson model, we have

$$\begin{aligned} \hat{H}_{\text{HN}} &= \sum_i (t_L c_i^\dagger c_{i+1} + t_R c_{i+1}^\dagger c_i) \\ &= \sum_{k_x \in (-\pi, \pi)} a_{k_x}^\dagger (v_{\text{eff}} \sin k_x + i\zeta \cos k_x) a_{k_x}, \end{aligned} \quad (20)$$

where $t_L = (v_{\text{eff}} - \zeta)/2$ and $t_R = (v_{\text{eff}} + \zeta)/2$. According to the 1D Hatano-Nelson model, the localization length in non-Hermitian Haldane model is described by

$$\xi = \frac{c}{2 \ln \frac{t_R}{t_L}}, \quad (21)$$

where $c = \sqrt{3}a$ and a is lattice constant of Haldane model.

The characteristics of the complex spectrum under edge dissipation are discussed. The numerical results given by the non-Hermitian Haldane model match our effective model (half of the Hatano-Nelson). As shown in Fig. 3(a), the red line represents the numerical energy levels of the topological edge states under PBC and the cobalt blue stars represent the numerical energy levels of the 1D Hatano-Nelson model. By comparing the energy levels, it is found that the effective model of chiral modes at $y = 0$ is only half of a 1D Hatano-Nelson model, which is the negative imaginary parts of the energy levels of the 1D Hatano-Nelson model. Moreover, the numerical results of the particle distribution of topological edge states matches our analytical prediction based on Eq. (19) [Fig. 3(d)]. The inset in Fig. 3(d) illustrates that the numerical results for the localization length ξ correspond to the localization length of the half Hatano-Nelson model [Eq. (21)].

The localization behavior of topological edge states under edge dissipation is investigated using the NHCSE. Firstly, we introduce uniform dissipation on the outermost edge at $y = 0$ with $\gamma_i = -0.1t_1$, as shown in Fig. 3(a). The complex spectrum reveals that the chiral edge states on the dissipative edge exhibit non-zero effective dissipation. Next, we consider an asymmetric dissipation configuration on the outermost edge ($y = 0$), where one half of the system has dissipation $\gamma(x < 0) = -0.1t_1$, and the other half has dissipation $\gamma(x > 0) = 0.1t_1$, as depicted in Fig. 3(b). By utilizing the NHCSE theory, we predict the emergence of A-type GDDWs on the dissipative edge at $x = 0$, which are associated with the direction of chiral current $v_x < 0$ at the edge $y = 0$. The numerical results of the particle distribution, as depicted in Fig. 3(c), confirm the localization of chiral edge states at the A-type GDDWs, thus validating the theoretical predictions.

Therefore, NHCSE can be considered as “*anomaly*” NHSE and only is realized on the boundaries (or certain DWs) of a 2D Chern insulator.

B. The Non-Local Effect of NHCSE

Second, we discuss the interplay between the topological edge states on both edges (the edge with dissipation and that without) and show the non-local effect of NHCSE. We consider a non-Hermitian Haldane model on a strip with zigzag edges, of which one edge has dissipation ($y = 0$) and the other has not ($y = L_y$). The distance between two edges is set to be L_y , as shown in Fig. 4(a).

We consider the GDDWs on the edge ($y = 0$). In the limit of $L_y \rightarrow \infty$ (for example, $L_y = 40$), the results look trivial — due to NHCSE, the topological edge states on the edge with GDDWs become localized on GDDWs; the topological edge states on the edge without dissipation are extended, as shown in Fig. 4(a). In the scenario

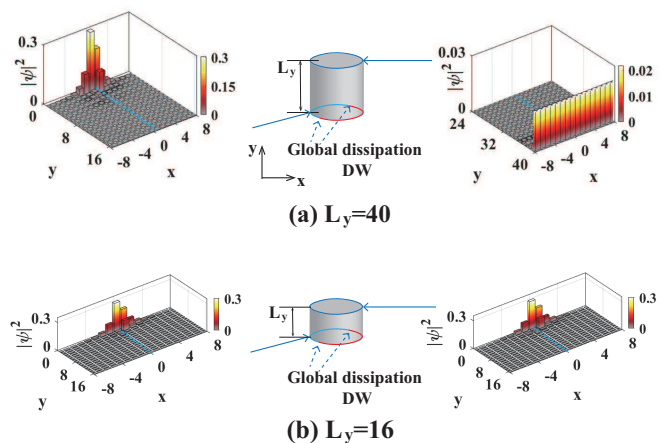


FIG. 4: The non-local NHCSE. The nanoribbons of the Haldane model with a pair of GDDW on a single outermost zigzag edge ($y = 0$) ($\gamma_R(x > 0) = 0.5t_1$, $\gamma_L(x < 0) = -0.5t_1$). (a) The topological edge states on edge ($y = 0$) are localized on the GDDW, and the other on edge ($y = L_y$) are extended on its corresponding edge. (b) The topological edge states on both edges ($y = 0, y = L_y$) are localized on the GDDW.

where L_y has a small value (for example, $L_y = 16$), an unusual occurrence takes place whereby the topological edge states on the edge with dissipation as well as the ones on the edge without it *both* become localized on the same GDDWs. To emphasize the results, we call it *non-local NHCSE*, as shown in Fig. 4(b). In the future, we will study the mechanism for non-local NHCSE and try to give a reasonable answer.

VI. APPLICATION: MECHANISM OF HYBRID SKIN-TOPOLOGICAL EFFECT IN CHERN INSULATORS

In this section, we explain the mechanism of the gain/loss-induced hybrid skin-topological effect and demonstrate that this effect can be understood in terms of multiple GDDWs for topological edge states in the theory of NHCSE. Specifically, we focus on the non-Hermitian Haldane model and the staggered on-site gain/loss can be expressed as

$$\delta\hat{H}_D = i\gamma \sum_i c_{A,i}^\dagger c_{A,i} - i\gamma \sum_i c_{B,i}^\dagger c_{B,i}, \quad (22)$$

where A/B are the two sublattice sites in each subcell and γ denotes the strength of dissipation. It holds significant importance as it is firstly proposed the gain/loss-induced hybrid skin-topological effect[37].

In our study, NHCSE is the origin of the hybrid skin-topological effect, which arises from the presence of global effective dissipation at the boundaries. Next, we will demonstrate that staggered on-site gain/loss throughout the entire system can be equivalently regarded as effective dissipation at the boundaries for topological edge states.

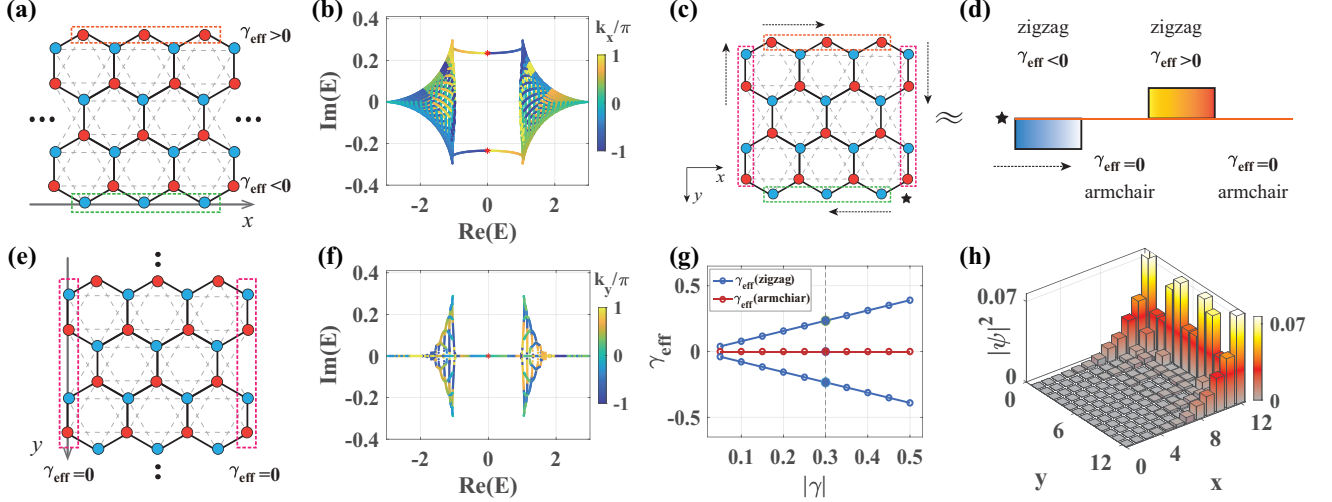


FIG. 5: Illustration of NHCSE with staggered gain/loss. (a),(e) Schematic diagram of the non-Hermitian Haldane model with zigzag edges(a) and armchair edges(e). The orange boxes represent regions of effective gain, the green boxes represent regions of effective loss, and the magenta boxes represent regions without dissipation. (b),(f) Energy levels in the complex spectrum for zigzag edges(b) and armchair edges(f). The red stars represent the effective dissipation on each edge. (c) Schematic diagram of the non-Hermitian Haldane model under OBC with zigzag and armchair edges. The dotted arrows indicate the direction of the chiral current. (d) Schematic diagram multi-GDDWs with the direction of the chiral current $v > 0$, which is equivalent to (c). (g) Variation of effective edge dissipation on the zigzag and armchair edges for varying strengths of γ . (h) Spatial distribution of particles in the topological edge states corresponding to the configuration in (c). The strength of gain/loss is $|\gamma| = 0.3t_1$.

To obtain the effective dissipation at each boundary, we consider two cylindrical Haldane systems in PBC along the x direction and OBC along the y direction (x PBC/ y obc) with zigzag edges [Fig. 5(a)], and x OBC/ y PBC with armchair edges [Fig. 5(e)]. The effective edge dissipation with zigzag edges for topological edge states is given by

$$\begin{aligned} \gamma_{\text{eff}}^{\text{zigzag}} = & \text{Im} \langle \psi_{\text{edge}}(k_x) | (i\gamma \sum_i c_{A,i}^\dagger c_{A,i} \\ & - i\gamma \sum_i c_{B,i}^\dagger c_{B,i}) | \psi_{\text{edge}}(k_x) \rangle, \end{aligned} \quad (23)$$

and the effective edge dissipation with armchair edges for topological edge states is given by

$$\begin{aligned} \gamma_{\text{eff}}^{\text{armchair}} = & \text{Im} \langle \psi_{\text{edge}}(k_y) | (i\gamma \sum_i c_{A,i}^\dagger c_{A,i} \\ & - i\gamma \sum_i c_{B,i}^\dagger c_{B,i}) | \psi_{\text{edge}}(k_y) \rangle, \end{aligned} \quad (24)$$

where ψ_{edge} denote topological edge states. As shown in Fig. 5(b) and (f), We plot the complex energy spectrum for the case of zigzag edges [Fig. 5(b)] and armchair edges [Fig. 5(f)]. In the energy spectrum, the effective dissipation associated with chiral modes on the two edges are indicated by red stars. For the topological edge states on the zigzag edge, where there is no symmetry between the A and B sub-lattices, the contributions do not cancel out, leading to a non-zero effective dissipation. However, on the armchair edge, the contributions from the A and B sub-lattices cancel out due to their symmetry, resulting in zero effective dissipation. The effective dissipation

on the zigzag and armchair edges [Fig. 5(a) and (e)] as a function of γ are depicted in Fig. 5(g). This finding illustrates that the skin effect induced by the global staggered on-site gain/loss can be effectively described as a theoretical model of NHCSE, which is determined by effective dissipation at the boundaries.

As previously discussed, the hybrid skin-topological effect induced by staggered gain/loss is determined by the effective dissipation at the boundaries. Due to chiral edge currents propagating along the geometric boundaries of the system under OBC, it suggests that chiral edge states are determined by the effective dissipation on the system's geometric boundaries. To explain the mechanism of the hybrid skin-topological effect under OBC [Fig. 5(c)] to the multi-GDDWs issue in the framework of NHCSE [Fig. 5(d)]. Here, we provide a specific system with rectangular borders to illustrate the skin effect of topological edge states.

In the case of OBC with rectangular borders, the effective dissipation along the four edges can be obtained as shown in Fig. 5(g), corresponding to $-\gamma_{\text{eff}}^{\text{zigzag}}, 0, \gamma_{\text{eff}}^{\text{zigzag}}, 0$, respectively. This mapping successfully transforms the case of OBC with rectangular borders in Fig. 5(c) into the multi-GDDWs model depicted in Fig. 5(d). By analyzing the multi-GDDWs model of NHCSE, we explain the hybrid skin-topological effect under OBC with rectangular borders. In Fig. 5(d), the direction of chiral current is positive ($v > 0$), based on Eq. (3) and continuity condition at each GDDW, the wave function increases along the x -axis in the region where $\gamma_{\text{eff}} - \bar{\gamma} > 0$, decreases in the region where $\gamma_{\text{eff}} - \bar{\gamma} < 0$, and extended

in the region where $\gamma_{\text{eff}} - \bar{\gamma} = 0$. In addition, Fig. 5(h) provides evidence supporting our theory. It shows the extension of chiral edge states at the armchair boundary, where the effective dissipation is zero. Conversely, at the zigzag boundary, the chiral edge states exhibit localization in a specific direction, indicative of the skin effect. Further detailed derivations for the solutions of the multi-GDDWs model can be found in Appendix D.

In summary, we conclude that NHCSE is the mechanism behind the hybrid skin-topological effect in Chern insulators, distinguishing it from 1D chain NHSE or higher-order NHSE. Our findings demonstrate that hybrid skin-topological effect can be observed by introducing inhomogeneous effective dissipation at the system boundaries.

VII. REALIZATION OF AN ELECTRIC CIRCUIT IN HALDANE MODEL WITH GLOBAL DISSIPATION DOMAIN WALL

In this section, we present a circuit design that implements the non-Hermitian Haldane model with global dissipation domain walls.

Our experimental platform utilizes an LC circuit combined with resistors (R_-) and negative resistors (INIC) (R_+) to observe NHCSE in the non-Hermitian Haldane model with GDDW. To map the Haldane model with GDDW onto the electric circuit, we introduce various types of couplings[60, 61] and on-site gain/loss[62]. Three charts in Fig. 6 illustrate the circuit implementations of nearest-neighbor (NN) hopping[Fig.6(c)], next-nearest-neighbor (NNN) hopping[Fig.6(d)], and GDDWs[Fig.6(b)]. In Fig.6(c) and (d), the gray dotted box represents a lattice site in a tight-binding model, containing two inductors (X, Y). The voltages between the inductors, denoted as U_X and U_Y , are used to define the variables $U_{\uparrow,\downarrow} = U_X \pm iU_Y$. By applying Kirchhoff's law and utilizing this notation, we derive the eigenequation for the spin-up and spin-down states

$$E \begin{bmatrix} U_{\mathbf{k},\uparrow}^A \\ U_{\mathbf{k},\uparrow}^B \end{bmatrix} = \begin{bmatrix} p_{\mathbf{k}}(\varphi) - M_A & T_{\mathbf{k}} \\ T_{\mathbf{k}}^* & p_{\mathbf{k}}(-\varphi) - M_B \end{bmatrix} \begin{bmatrix} U_{\mathbf{k},\uparrow}^A \\ U_{\mathbf{k},\uparrow}^B \end{bmatrix}, \quad (25)$$

where the energy is characterised by $E = 3t_1 + 6t_2 - \frac{2w_0^2}{w^2}$, the NNN hopping is characterised by $p_{\mathbf{k}}(\varphi) = 2t_2 [\cos(\mathbf{k} \cdot \mathbf{v}_1 + \varphi) + \cos(\mathbf{k} \cdot \mathbf{v}_2 + \varphi) + \cos(\mathbf{k} \cdot \mathbf{v}_3 + \varphi)]$, the NN hopping is characterised by $T_{\mathbf{k}} = t_1(e^{i\mathbf{k}\mathbf{e}_1} + e^{i\mathbf{k}\mathbf{e}_2} + e^{i\mathbf{k}\mathbf{e}_3})$, and the on-site term is characterised by $M_{A(B)} = (C_g - \frac{1}{w^2 L_g} - \frac{i}{w R_{g,A(B)}})/C$. The specific derivations can be found in Appendix E. For convenience, the grounding capacitance and inductance are set as $C_g = C$, $L_g = L$, and capacitance representing coupling is set as $C_1 = t_1 C$, $C_2 = t_2 C$.

The eigenfrequency of circuit is $\omega_0 = 1/(LC)^{1/2}$, and Eq. (25) is the eigenequation of the non-Hermitian Haldane

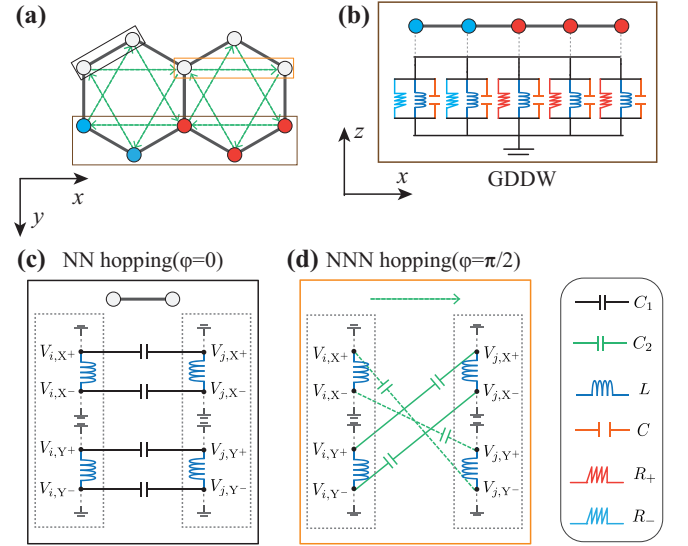


FIG. 6: The schematic of the designed electric circuit. (a) Illustration of non-Hermitian Haldane model. The brown box indicates the GDDW shown in (b), the black box indicates the NN hopping shown in (c), and the orange box indicates the NNN hopping shown in (d). (b) The circuit implementation of the GDDW. (c) Schematic of the circuit implementation of the NN hopping. (d) Schematic of the circuit implementation of the NNN hopping.

model. Notably, the on-site dissipation is described as

$$i\gamma_{A(B)} = -M_{A(B)} = -\frac{i}{R_{g,A(B)}} \sqrt{\frac{L}{C}}. \quad (26)$$

It's to be noted that $R_{g,A(B)}$ can be negative by using INIC, which corresponded to gain in the non-Hermitian Haldane model. We show more details in Appendix E.

Let us now consider the electric circuit that has PBC along the x direction, and an OBC along the y direction with zigzag edges, the NN and NNN coupling is grounded at $y = 0$ and $y = L$. To achieve a pair of GDDWs, we utilize two approaches. In the first approach, we place half of the resistors with a value of R_1 and half of the resistors with a value of R_2 at the corresponding grid points on the boundary. Alternatively, in the second approach, we position half of the resistors with a value of R_1 and an equal number of the same type of INIC at the corresponding grid points on the boundary. These strategies enable us to create the GDDW and facilitate the desired dissipation distribution. In semi-infinite case, the voltage distribution at the eigenfrequency ω_0 is measured to obtain the corresponding eigenvalue E , and the eigenstate $[U_{\mathbf{k},\uparrow}^A, U_{\mathbf{k},\uparrow}^B]^T$. These simulation experiments are convenient and clear to observe the NHCSE phenomenon.

VIII. CONCLUSION

In the end, we answer the three questions at the beginning: (i) We found a fundamental difference between the NHSE for bulk states and NHCSE for topological

edge states with inhomogeneous dissipation. One key point is that NHCSE is a “NHSE” under PBC rather than OBC. The chiral modes localize around GDDWs – a special topological defect of global dissipation rather than the boundaries of the systems. Another key point is “anomaly”. For example, the NHCSE for topological edge states is characterized by half of the Hatano-Nelson model rather than a whole 1D tight-binding lattice model. The specific distinctions are shown in Fig. 7. (ii) We found that without point-like topological configuration, NHCSE is characterized by the “global dissipation” γ_{global} rather than a certain “winding number”. (iii) We have a deeper understanding of the hybrid skin-topological effect in Chern insulators with the help of NHCSE in multiple GDDWs for topological edge states. In summary, we conclude that

Chiral modes + Inhomogeneous dissipation
 → Non-Hermitian chiral skin effect.

In the future, we will try to systematically understand the interplay of non-Hermitian physics and topological quantum states by studying the NHCSE for topological edge states in other types of topological quantum states, such as higher-order Chern insulators, topological superconductors, and topological semi-metals.

Properties	Traditional NHSE	Non-Hermitian chiral skin effect
Boundary condition	Open boundary condition	Period boundary condition
Normal/Anomalous	Normal	Anomalous: Cannot be observed in a one-dimensional model
Localized position	All eigenstates are localized at the system boundary	Chiral edge states are localized at the global dissipative domain walls
Topological Invariant / “order parameter” for NHSE	Winding number in complex energy space	Global dissipation: the effect of subtracting the average dissipation from the spatial distribution of dissipation
Energy spectrum structure	Form a closed loop	Chiral states form a straight line with fixed imaginary part in complex energy space

FIG. 7: The schematic of the difference between traditional NHSE and NHCSE.

ACKNOWLEDGMENTS

This work was supported by the Natural Science Foundation of China (Grants No. 11974053 and No. 12174030). We are grateful to Zhong Wang, Chen Fang, Lin-Hu Li, Wei Yi, Gao-yong Sun, Ya-jie Wu, Can Wang, Fei Yang, Xian-qi Tong, and Yue Hu for helpful discussions that contributed to clarifying some aspects related to the present work.

Appendix A: The Wave Functions of Chiral Edge States with Dissipation $\gamma(x)$

The effective edge model of the topological edge states is given by the Hamiltonian

$$\hat{H} = vk + i\gamma(x), \quad (\text{A1})$$

or

$$\hat{H} = -iv\frac{d}{dx} + i\gamma(x), \quad (\text{A2})$$

where $x \in [0, L]$, v is the velocity of the edge states, k is the wavenumber, and $\gamma(x)$ represents the dissipation as a function of position x .

To obtain the wave function of the topological edge states, we consider the stationary Schrodinger equation

$$[-iv\frac{d}{dx} + i\gamma(x)]\psi(x) = E\psi(x), \quad (\text{A3})$$

where E is the energy of the system. Solving this equation, we obtain the wave function

$$\psi(x) = \frac{1}{\mathcal{N}} e^{i\frac{E}{v}x} e^{\frac{1}{v} \int \gamma(x) dx}, \quad (\text{A4})$$

where \mathcal{N} is the normalization factor. Here, E can be any complex number.

To determine the energy E , we impose PBC $\psi(0) = \psi(L)$, which yield

$$i\frac{E}{v}L + \frac{1}{v} \int_0^L \gamma(x) dx = i2\pi n, \quad (\text{A5})$$

where $n \in \mathbb{Z}$. This equation gives us the energy of the edge states, which can be expressed as

$$E = vk + i\bar{\gamma}, \quad (\text{A6})$$

where $k = \frac{2\pi n}{L}$, and $\bar{\gamma} = \frac{1}{L} \int_0^L \gamma(x) dx$. Substituting this expression for E into the wave function, we obtain

$$\psi_k(x) = \frac{1}{\mathcal{N}} e^{ikx} e^{\frac{1}{v} \int_0^x [\gamma(x) - \bar{\gamma}] dx}. \quad (\text{A7})$$

This equation describes the wave function of the edge states for a given wavenumber k . We define global dissipation as $\gamma_{\text{global}}(x) = \gamma(x) - \bar{\gamma}$, where $\bar{\gamma}$ is the average value of inhomogeneous dissipation $\bar{\gamma} = \frac{1}{L} \int_0^L \gamma(x) dx$.

Appendix B: Proof of the Relationship between Wave Function Localization and the Existence of GDDWs

Definition 1: x_0 is called an A -type GDDW on the interval $[a, b]$. We always make a and b belong to $[0, L]$ by changing the initial point, if there exist three positive real numbers, $a < x_0 < b$, such that for any x_L satisfying

$a < x_L < x_0$, $\gamma_{global}(x_L) < 0$, and for any x_R satisfying $x_0 < x_R < b$, $\gamma_{global}(x_R) > 0$.

Definition 2: x_0 is called a B-type GDDW on the interval $[a, b]$. We always make a and b belong to $[0, L]$ by changing the initial point, if there exist three positive real numbers, $a < x_0 < b$, such that for any x_L satisfying $a < x_L < x_0$, $\gamma_{global}(x_L) > 0$, and for any x_R satisfying $x_0 < x_R < b$, $\gamma_{global}(x_R) < 0$.

Definition 3: The wave function is said to be localized at x_0 within the interval $[a, b]$ if the squared modulus of the wave function is monotonically increasing in the interval $[a, x_0)$ and monotonically decreasing in the interval $(x_0, b]$ when $a < x_0 < b$.

Theorem: If $\gamma_{global}(x)$ is a continuous function, then a chiral mode with a negative speed is localized at x_0 (within a certain interval) if and only if there exists a type-A GDDW at x_0 . Furthermore, a chiral mode with a positive speed is localized at x_0 (within a certain interval) if and only if there exists a type-B GDDW at x_0 .

Proof:

Sufficiency: We first prove that the existence of an A-type GDDW or a B-type GDDW implies the localization of the corresponding chiral mode.

Assume we have an A-type GDDW at x_0 . According to Definition 1, for any x_L satisfying $a < x_L < x_0$, we have $\gamma_{global}(x_L) < 0$, and for any x_R satisfying $x_0 < x_R < b$, we have $\gamma_{global}(x_R) > 0$. The squared modulus of the wave function is

$$|\psi_k(x)|^2 = \frac{1}{\mathcal{N}^2} e^{\frac{2}{v} \int_0^x \gamma_{global}(x') dx'} > 0. \quad (\text{B1})$$

We now find the derivative of the squared modulus for x . Based on Equation (B1), due to $\gamma_{global}(x)$ is a continuous function, we obtain:

$$\frac{d|\psi_k(x)|^2}{dx} = \frac{2}{v} |\psi_k(x)|^2 \gamma_{global}(x). \quad (\text{B2})$$

Since $\gamma_{global}(x_L) < 0$ and $\gamma_{global}(x_R) > 0$, according to Equation (B2), we deduce that:

$$\begin{aligned} \text{sign}(v) \frac{d|\psi_k(x_L)|^2}{dx} < 0, & \quad \text{in the interval } [a, x_0), \\ \text{sign}(v) \frac{d|\psi_k(x_R)|^2}{dx} > 0, & \quad \text{in the interval } (x_0, b]. \end{aligned} \quad (\text{B3})$$

This means that for the chiral mode with a negative speed, the squared modulus is monotonically increasing in the interval $[a, x_0)$ and monotonically decreasing in the interval $(x_0, b]$. Thus, the chiral mode with negative speed will be localized at x_0 .

Similarly, assume we have a B-type GDDW at x_0 . According to Definition 2, for any x_L satisfying $a < x_L < x_0$, we have $\gamma_{global}(x_L) > 0$, and for any x_R satisfying $x_0 < x_R < b$, we have $\gamma_{global}(x_R) < 0$. Using the same arguments as before with the derivative of the squared modulus in Equation (B2), we can conclude that the squared modulus is monotonically increasing in the interval $[a, x_0)$ and monotonically decreasing in the interval $(x_0, b]$. Consequently, the chiral mode with positive

speed will be localized at x_0 provided we have a B-type GDDW.

Necessity: Now, we prove that the localization of chiral modes can only occur if there is an A-type or B-type GDDW.

Assume a chiral mode with negative speed is localized at x_0 . Based on Definition 3, the squared modulus of the wave function should be monotonically increasing in the interval $[a, x_0]$ and monotonically decreasing in the interval $[x_0, b]$ when $a < x_0 < b$. Thus, we know that for x in the interval $[a, x_0)$:

$$\frac{d|\psi_k(x)|^2}{dx} > 0. \quad (\text{B4})$$

Equation (B4) implies $\text{sign}(v)\gamma_{global}(x) > 0$ for all x in the interval $[a, x_0)$. Similarly, for x in the interval $(x_0, b]$:

$$\frac{d|\psi_k(x)|^2}{dx} < 0. \quad (\text{B5})$$

This constraint implies $\text{sign}(v)\gamma_{global}(x) < 0$ for all x in the interval $(x_0, b]$. Combining these results, we conclude that an A-type GDDW must exist if the chiral mode with negative speed is localized.

Likewise, if a chiral mode with negative speed is localized at x_0 , by following the same logic, we can conclude that a B-type GDDW must exist for a localized chiral mode with positive speed.

Appendix C: Non-Hermitian chiral skin effect with a pair of uniform GDDW

we consider a pair of GDDW that separates the regions with different strengths of dissipation in the left or right region. The uniform GDDW is set as

$$\gamma_L(0 < x < L_1) = \gamma_1; \gamma_R(L_1 < x < L) = \gamma_2 \quad (\text{C1})$$

where γ_R and γ_L are the dissipation strengths in the right and left regions, respectively. Then we have

$$\bar{\gamma} = \frac{1}{L} \int_0^L \gamma(x) dx = \frac{\gamma_1 \cdot L_1 + \gamma_2 \cdot (L - L_1)}{L} \quad (\text{C2})$$

Corroding to Eq. (A7), in the left region $x \in [0, L_1]$, we have

$$\begin{aligned} \psi^{(1)}(x) &= \frac{1}{\mathcal{N}_1} e^{ikx} e^{\frac{1}{v} \int_0^x [\gamma(x) - \bar{\gamma}] dx} \\ &= \frac{1}{\mathcal{N}_1} e^{ikx} e^{\alpha_1 x} \end{aligned} \quad (\text{C3})$$

where $\alpha_1 = \frac{(\gamma_1 - \gamma_2) \cdot (L - L_1)}{vL}$. In the right region $x \in [L_1, L]$, we have

$$\begin{aligned} \psi^{(2)}(x) &= \frac{1}{\mathcal{N}_2} e^{ikx} e^{\frac{1}{v} \int_{L_1}^x [\gamma(x) - \bar{\gamma}] dx} \\ &= \frac{1}{\mathcal{N}_2} e^{ikx} e^{\alpha_2(x - L_1)} \end{aligned} \quad (\text{C4})$$

where $\alpha_2 = \frac{(\gamma_2 - \gamma_1) \cdot L_1}{vL}$. Applying the boundary conditions $\psi^{(1)}(0) = \psi^{(2)}(L)$, $\psi^{(1)}(L_1) = \psi^{(2)}(L_1)$, we set $\mathcal{N}_1 = e^{\alpha_1 \cdot L_1}$, $\mathcal{N}_2 = 1$. Finally, we have

$$\psi^{(1)}(x) = \frac{1}{e^{\alpha_1 \cdot L_1}} e^{ikx} e^{\frac{(\gamma_1 - \gamma_2) \cdot (L - L_1)}{v} x} \quad (\text{C5})$$

$$\psi^{(2)}(x) = e^{ikx} e^{\frac{(\gamma_2 - \gamma_1) \cdot L_1}{v} (x - L_1)} \quad (\text{C6})$$

For the case of $L_1 = L/2$, $\gamma_L(0 < x < L/2) = \gamma_1$; $\gamma_R(L/2 < x < L) = \gamma_2$, we have $\alpha_1 = \frac{\gamma_1 - \gamma_2}{2v}$ and $\alpha_2 = \frac{\gamma_2 - \gamma_1}{2v}$. The wave function of the edge states for a given wavenumber k in the presence of the domain wall is given by

$$\psi^{(1)}(x) = \frac{1}{e^{\frac{(\gamma_1 - \gamma_2) \cdot L}{4v}}} e^{ikx} e^{\frac{\gamma_1 - \gamma_2}{2v} x} \quad (\text{C7})$$

$$\psi^{(2)}(x) = e^{ikx} e^{\frac{\gamma_2 - \gamma_1}{2v} (x - L/2)} \quad (\text{C8})$$

where ξ is the localization length, which is given by

$$\xi = \frac{2v}{|\gamma_R - \gamma_L|}. \quad (\text{C9})$$

The following is a discussion of the specific physical implications of this example.

Example 1: The effective model corresponds to Fig. 2(a) and Fig. 3(b) in the main text. The parameters are set as $L_1 = L/2$, $\gamma_L(0 < x < L/2) = -\gamma$, $\gamma_R(L/2 < x < L) = \gamma$.

In this case, $\alpha_1 = -\frac{\gamma}{v}$ and $\alpha_2 = \frac{\gamma}{v}$. The wave function of the edge states for a given wavenumber k in the presence of the domain wall is given by

$$\psi^{(1)}(x) = \frac{1}{e^{\frac{\gamma L}{2v}}} e^{ikx} e^{-\frac{\gamma}{v} x} \quad (\text{C10})$$

$$\psi^{(2)}(x) = e^{ikx} e^{\frac{\gamma}{v} (x - L/2)} \quad (\text{C11})$$

where ξ is the localization length, which is given by

$$\xi = \frac{v}{\gamma}. \quad (\text{C12})$$

Example 2: The effective model corresponds to Fig. 2(b) in the main text. The parameters are set as $L_1 = L/2$, $\gamma_L(0 < x < L/2) = -\gamma$, $\gamma_R(L/2 < x < L) = 0$. In this case, $\alpha_1 = -\frac{\gamma}{2v}$ and $\alpha_2 = \frac{\gamma}{2v}$. The wave function of the edge states for a given wavenumber k in the presence of the domain wall is given by

$$\psi^{(1)}(x) = \frac{1}{e^{\frac{\gamma L}{2v}}} e^{ikx} e^{-\frac{\gamma}{2v} x} \quad (\text{C13})$$

$$\psi^{(2)}(x) = e^{ikx} e^{\frac{\gamma}{2v} (x - L/2)} \quad (\text{C14})$$

where ξ is the localization length, which is given by

$$\xi = \frac{2v}{\gamma}. \quad (\text{C15})$$

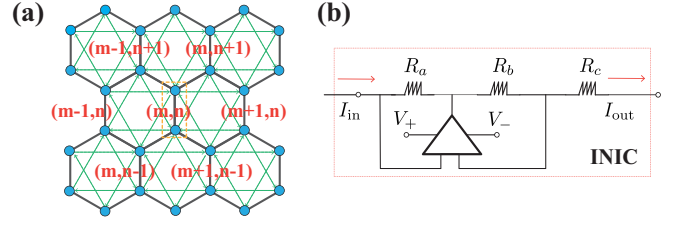


FIG. 8: (a) Schematic of the non-Hermitian Haldane model with uniform dissipation in bulk in the designed circuit. (b) The schematic diagram of an electrical circuit for realizing the negative resistance.

Appendix D: Non-Hermitian chiral skin effect with multiple GDDWs

In this part, we consider multiple uniform GDDWs that divide into n regions based on different strengths of dissipation. System total length is L , with a dissipation of γ_1 over a length of L_1 , a dissipation of γ_2 over a length of L_2 , and a dissipation of γ_n over a length of L_n . The uniform GDDW is set as $\gamma(0 < x < L_1) = \gamma_1$; $\gamma(L_1 < x < L_2 + L_1) = \gamma_2$; \dots ; $\gamma(L - L_n < x < L) = \gamma_n$, where $\sum_n L_n = L$. Then we have

$$\begin{aligned} \bar{\gamma} &= \frac{1}{L} \int_0^L \gamma(x) dx \quad (\text{D1}) \\ &= \frac{\gamma_1 \cdot L_1 + \gamma_2 \cdot L_2 + \gamma_3 \cdot L_3 + \dots + \gamma_n \cdot L_n}{L} \end{aligned}$$

where

$$\alpha_1 = -\frac{\gamma_1 \cdot (L_1 - L) + \gamma_2 \cdot L_2 + \gamma_3 \cdot L_3 + \dots + \gamma_n \cdot L_n}{vL} \quad (\text{D2})$$

$$\alpha_2 = -\frac{\gamma_1 \cdot L_1 + \gamma_2 \cdot (L_2 - L) + \gamma_3 \cdot L_3 + \dots + \gamma_n \cdot L_n}{vL} \quad (\text{D3})$$

$$\alpha_n = -\frac{\gamma_1 \cdot L_1 + \gamma_2 \cdot L_2 + \gamma_3 \cdot L_3 + \dots + \gamma_n \cdot (L_n - L)}{vL} \quad (\text{D4})$$

According to Eq. (A7), the wave function is given

$$\psi^{(1)}(x) = \frac{1}{\mathcal{N}_1} e^{ikx} e^{\alpha_1 x} \quad (\text{D5})$$

$$\psi^{(2)}(x) = \frac{1}{\mathcal{N}_2} e^{ikx} e^{\alpha_2 (x - L_1)} \quad (\text{D6})$$

$$\psi^{(n)}(x) = \frac{1}{\mathcal{N}_n} e^{ikx} e^{\alpha_n (x - L_{n-1})} \quad (\text{D7})$$

According to continuous condition, $\psi^{(1)}(0) = \psi^{(n)}(L)$, $\psi^{(1)}(L_1) = \psi^{(2)}(L_1)$, $\psi^{(2)}(L_2) = \psi^{(3)}(L_2)$, \dots , $\psi^{(n-1)}(L_{n-1}) = \psi^{(n)}(L_{n-1})$. Finally, we can get

$$\mathcal{N}_n = e^{-\sum_{i=n-1, i \in \mathbb{N}^+} [\alpha_i \cdot (L_i - L_{i-1})]} \quad (\text{D8})$$

where $\mathcal{N}_1 = 1$, and $L_0 = 0$.

The following is a discussion of the specific multi-GDDWs in Fig. 5(d). The parameters are set as $L_i = L/4$ ($i \in \{1, 2, 3, 4\}$), $\gamma_1(0 < x < L/4) = \gamma_{\text{eff}}^{\text{zigzag}} = -\gamma$, $\gamma_2(L/4 < x < L/2) = \gamma_{\text{eff}}^{\text{armchair}} = 0$, $\gamma_3(L/2 < x < 3L/4) = \gamma_{\text{eff}}^{\text{zigzag}} = \gamma$, $\gamma_4(3L/4 < x < L) = \gamma_{\text{eff}}^{\text{armchair}} = 0$.

In this case, $\alpha_1 = -\frac{3\gamma}{4v}$, $\alpha_3 = \frac{3\gamma}{4v}$, and $\alpha_2 = \alpha_4 = 0$. The wave function of the edge states for a given wavenumber k in the presence of the domain wall is given by

$$\psi^{(1)}(x) = e^{ikx} e^{-\frac{3\gamma}{4v}x} \quad (\text{D9})$$

$$\psi^{(2)}(x) = \psi^{(4)}(x) = e^{ikx} \quad (\text{D10})$$

$$\psi^{(3)}(x) = e^{-\frac{3\gamma L}{16v}} e^{ikx} e^{\frac{3\gamma}{4v}(x-L/2)} \quad (\text{D11})$$

where ξ is the localization length on zigzag edges, which is given by

$$\xi = \frac{4v}{3\gamma}. \quad (\text{D12})$$

Appendix E: Theoretical model of the designed electric circuit

In this part, we theoretically demonstrate the correspondence between the non-Hermitian Haldane model with uniform dissipation in bulk and our designed electric circuit. Based on Kirchhoff's law, the relationship between current and voltage at node m is described by

$$I_m = \left[\sum_n i\omega C_{mn}(V_m - V_n) + \sum_n \frac{1}{i\omega L_{mn}}(V_m - V_n) + i\omega C_g V_m + \frac{V_m}{R_m} \right]. \quad (\text{E1})$$

where I_m and V_m are the net current and voltage of node m with angular frequency being ω . L_{mn} is the inductance between node m and node n . C_{mn} is the capacitance between node m and node n . The summation is taken over all nodes, which are connected to node m through an inductor or a capacitor. C_g is the ground capacitance at node m . R_m is the resistor or negative resistor at node m .

In PBC with loss in bulk, each lattice site possesses 4 nodes(X^+, X^-, Y^+, Y^-). In this case, the voltage and current at the site i should be written as: $V_i = [V_{i,X^+}, V_{i,X^-}, V_{i,Y^+}, V_{i,Y^-}]^T$ and $I_i = [I_{i,X^+}, I_{i,X^-}, I_{i,Y^+}, I_{i,Y^-}]^T$. Additionally, each site (grounded through C_g) is connected with other sites through two kinds of coupling: (three) NN couplings (C_1), (six) NNN couplings(C_2). Also, the NNN couplings are directional-dependent, and the coupling pattern determines the sign of the geometric phase $\varphi = \pi/2$.

In this case, the Kirchhoff equation on node $X^+(m, n, A)$ can be expressed as:

$$\begin{aligned} I_{m,n,X^+} &= (i\omega C_g + \frac{1}{i\omega L_g} + \frac{1}{R_{g,A}})V_{m,n,X^+}^A + \frac{1}{i\omega L}(V_{m,n,X^+}^A - V_{m,n,X^-}^A) \\ &+ i\omega C_1 \left[(V_{m,n,X^+}^A - V_{m,n,X^+}^B) + (V_{m,n,X^+}^A - V_{m,n-1,X^+}^B) + (V_{m,n,X^+}^A - V_{m+1,n-1,X^+}^B) \right] \\ &+ i\omega C_2 \left[(V_{m,n,X^+}^A - V_{m+1,n-1,Y^-}^A) + (V_{m,n,X^+}^A - V_{m,n-1,Y^+}^A) + (V_{m,n,X^+}^A - V_{m,n+1,Y^-}^A) \right]. \end{aligned} \quad (\text{E2})$$

The Kirchhoff equation on node X^- can be expressed as

$$\begin{aligned} I_{m,n,X^-} &= (i\omega C_g + \frac{1}{i\omega L_g} + \frac{1}{R_{g,A}})V_{m,n,X^-}^A + \frac{1}{i\omega L}(V_{m,n,X^-}^A - V_{m,n,X^+}^A) \\ &+ i\omega C_1 \left[(V_{m,n,X^-}^A - V_{m,n,X^-}^B) + (V_{m,n,X^-}^A - V_{m,n-1,X^-}^B) + (V_{m,n,X^-}^A - V_{m+1,n-1,X^-}^B) \right] \\ &+ i\omega C_2 \left[(V_{m,n,X^-}^A - V_{m+1,n-1,Y^+}^A) + (V_{m,n,X^-}^A - V_{m,n-1,Y^-}^A) + (V_{m,n,X^-}^A - V_{m,n+1,Y^+}^A) \right]. \end{aligned} \quad (\text{E3})$$

We assume that there are no external sources so that the current flows out of each node is zero ($I_i = [I_{i,X^+}, I_{i,X^-}, I_{i,Y^+}, I_{i,Y^-}]^T = 0$). In this case, the Eq. (E3) becomes

$$\begin{aligned} 0 &= (i\omega C_g + \frac{1}{i\omega L_g} + \frac{1}{R_{g,A}} + 3i\omega C_1 + 6i\omega C_2)V_{m,n,X^+}^A + \frac{1}{i\omega L}(V_{m,n,X^+}^A - V_{m,n,X^-}^A) \\ &- i\omega C_1 (V_{m,n,X^+}^B + V_{m,n-1,X^+}^B + V_{m+1,n-1,X^+}^B) \\ &- i\omega C_2 (V_{m+1,n,Y^+}^A + V_{m-1,n,Y^-}^A + V_{m-1,n+1,Y^+}^A + V_{m+1,n-1,Y^-}^A + V_{m,n-1,Y^+}^A + V_{m,n+1,Y^-}^A), \end{aligned} \quad (\text{E4})$$

and

$$\begin{aligned}
0 = & (i\omega C_g + \frac{1}{i\omega L_g} + \frac{1}{R_{g,A}} + 3i\omega C_1 + 6i\omega C_2)V_{m,n,X^-}^A + \frac{1}{i\omega L}(V_{m,n,X^-}^A - V_{m,n,X^+}^A) \\
& - i\omega C_1(V_{m,n,X^-}^B + V_{m,n-1,X^-}^B + V_{m+1,n-1,X^-}^B) \\
& - i\omega C_2(V_{m+1,n,Y^-}^A + V_{m-1,n,Y^+}^A + V_{m-1,n+1,Y^-}^A + V_{m+1,n-1,Y^+}^A + V_{m,n-1,Y^-}^A + V_{m,n+1,Y^+}^A). \quad (\text{E5})
\end{aligned}$$

For convenience, the capacitance is set as $C_1 = t_1 C, C_2 = t_2 C$, where C acts as a reference capacitance. And we set $M_{A(B)} = (C_g - \frac{1}{\omega^2 L_g} + \frac{1}{i\omega R_{g,A(B)}})/C$. Each pair of the LC circuit has the same resonance frequency $\omega_0 = 1/\sqrt{LC}$.

We simply Eq. (E4) and Eq. (E5) as:

$$\begin{aligned}
V_{m,n,X^+}^A - V_{m,n,X^-}^A = & -\frac{\omega^2}{\omega_0^2}[-(M_A + 3t_1 + 6t_2)V_{m,n,X^+}^A + t_1(V_{m,n,X^+}^B + V_{m,n-1,X^+}^B + V_{m+1,n-1,X^+}^B) \\
& + t_2(V_{m+1,n,Y^+}^A + V_{m-1,n,Y^-}^A + V_{m-1,n+1,Y^+}^A + V_{m+1,n-1,Y^-}^A + V_{m,n-1,Y^+}^A + V_{m,n+1,Y^-}^A)], \quad (\text{E6})
\end{aligned}$$

and

$$\begin{aligned}
V_{m,n,X^-}^A - V_{m,n,X^+}^A = & -\frac{\omega^2}{\omega_0^2}[-(M_A + 3t_1 + 6t_2)V_{m,n,X^-}^A + t_1(V_{m,n,X^-}^B + V_{m,n-1,X^-}^B + V_{m+1,n-1,X^-}^B) \\
& + t_2(V_{m+1,n,Y^-}^A + V_{m-1,n,Y^+}^A + V_{m-1,n+1,Y^-}^A + V_{m+1,n-1,Y^+}^A + V_{m,n-1,Y^-}^A + V_{m,n+1,Y^+}^A)]. \quad (\text{E7})
\end{aligned}$$

The voltages across the inductors are set $U_X = V_{X^+} - V_{X^-}, U_Y = V_{Y^+} - V_{Y^-}$. The difference between Eqs. (E6) and (E7) yields

$$\begin{aligned}
U_{m,n,X}^A = & -\frac{\omega^2}{2\omega_0^2}[-(M_A + 3t_1 + 6t_2)U_{m,n,X}^A + t_1(U_{m,n,X}^B + U_{m,n-1,X}^B + U_{m+1,n-1,X}^B) \\
& + t_2(U_{m+1,n,Y}^A - U_{m-1,n,Y}^A + U_{m-1,n+1,Y}^A - U_{m+1,n-1,Y}^A + U_{m,n-1,Y}^A - U_{m,n+1,Y}^A)]. \quad (\text{E8})
\end{aligned}$$

We can also derive the equations for inductor Y at site A, as well as for site B following the same route:

$$\begin{aligned}
U_{m,n,Y}^A = & -\frac{\omega^2}{2\omega_0^2}[-(M_A + 3t_1 + 6t_2)U_{m,n,Y}^A + t_1(U_{m,n,Y}^B + U_{m,n-1,Y}^B + U_{m+1,n-1,Y}^B) \\
& + t_2(-U_{m+1,n,X}^A + U_{m-1,n,X}^A - U_{m-1,n+1,X}^A + U_{m+1,n-1,X}^A - U_{m,n-1,X}^A + U_{m,n+1,X}^A)], \quad (\text{E9})
\end{aligned}$$

$$\begin{aligned}
U_{m,n,X}^B = & -\frac{\omega^2}{2\omega_0^2}[-(M_B + 3t_1 + 6t_2)U_{m,n,X}^B + t_1(U_{m,n,X}^A + U_{m,n+1,X}^A + U_{m-1,n+1,X}^A) \\
& + t_2(-U_{m+1,n,Y}^B + U_{m-1,n,Y}^B - U_{m-1,n+1,Y}^B + U_{m+1,n-1,Y}^B - U_{m,n-1,Y}^B + U_{m,n+1,Y}^B)], \quad (\text{E10})
\end{aligned}$$

$$\begin{aligned}
U_{m,n,Y}^B = & -\frac{\omega^2}{2\omega_0^2}[-(M_B + 3t_1 + 6t_2)U_{m,n,Y}^B + t_1(U_{m,n,Y}^A + U_{m,n+1,Y}^A + U_{m-1,n+1,Y}^A) \\
& + t_2(U_{m+1,n,X}^B - U_{m-1,n,X}^B + U_{m-1,n+1,X}^B - U_{m+1,n-1,X}^B + U_{m,n-1,X}^B - U_{m,n+1,X}^B)]. \quad (\text{E11})
\end{aligned}$$

Defining $U_{\uparrow,\downarrow} = U_X \pm iU_Y$, we obtain

$$\begin{aligned}
(3t_1 + 6t_2 - \frac{2\omega_0^2}{\omega^2})U_{m,n,\uparrow}^A = & -M_A U_{m,n,\uparrow}^A + t_1(U_{m,n,\uparrow}^B + U_{m,n-1,\uparrow}^B + U_{m+1,n-1,\uparrow}^B) \\
& + t_2(e^{-i\varphi}U_{m+1,n,\uparrow}^A + e^{i\varphi}U_{m-1,n,\uparrow}^A + e^{-i\varphi}U_{m-1,n+1,\uparrow}^A \\
& + e^{i\varphi}U_{m+1,n-1,\uparrow}^A + e^{-i\varphi}U_{m,n-1,\uparrow}^A + e^{i\varphi}U_{m,n+1,\uparrow}^A), \quad (\text{E12})
\end{aligned}$$

and

$$\begin{aligned}
(3t_1 + 6t_2 - \frac{2w_0^2}{w^2})U_{m,n,\uparrow}^B &= -M_B U_{m,n,\uparrow}^B + t_1(U_{m,n,\uparrow}^A + U_{m,n+1,\uparrow}^A + U_{m-1,n+1,\uparrow}^A) \\
&+ t_2(e^{i\varphi}U_{m+1,n,\uparrow}^B + e^{-i\varphi}U_{m-1,n,\uparrow}^B + e^{i\varphi}U_{m-1,n+1,\uparrow}^B \\
&+ e^{-i\varphi}U_{m+1,n-1,\uparrow}^B + e^{i\varphi}U_{m,n-1,\uparrow}^B + e^{-i\varphi}U_{m,n+1,\uparrow}^B).
\end{aligned} \tag{E13}$$

where the geometric phase $\varphi = \pi/2$.

Consider NN coupling $U_{m,n}^B = e^{i\mathbf{k}e_1}U_{m,n}^A$, $U_{m+1,n-1}^B = e^{i\mathbf{k}e_2}U_{m,n}^A$, $U_{m,n-1}^B = e^{i\mathbf{k}e_3}U_{m,n}^A$, and NNN coupling $U_{m-1,n}^A = e^{i\mathbf{k}v_1}U_{m,n}^A$, $U_{m,n+1}^A = e^{i\mathbf{k}v_2}U_{m,n}^A$, $U_{m+1,n-1}^A = e^{i\mathbf{k}v_3}U_{m,n}^A$, we can get the independent equation for U_{\uparrow} as

$$E \begin{bmatrix} U_{\mathbf{k},\uparrow}^A \\ U_{\mathbf{k},\uparrow}^B \end{bmatrix} = \begin{bmatrix} p_{\mathbf{k}}(\varphi) - M_A & T_{\mathbf{k}} \\ T_{\mathbf{k}}^* & p_{\mathbf{k}}(-\varphi) - M_B \end{bmatrix} \begin{bmatrix} U_{\mathbf{k},\uparrow}^A \\ U_{\mathbf{k},\uparrow}^B \end{bmatrix}. \tag{E14}$$

where $E = 3t_1 + 6t_2 - \frac{2w_0^2}{w^2}$, $p_{\mathbf{k}}(\varphi) = 2t_2 [\cos(\mathbf{k} \cdot \mathbf{v}_1 + \varphi) + \cos(\mathbf{k} \cdot \mathbf{v}_2 + \varphi) + \cos(\mathbf{k} \cdot \mathbf{v}_3 + \varphi)]$, $T_{\mathbf{k}} = t_1(e^{i\mathbf{k}e_1} + e^{i\mathbf{k}e_2} + e^{i\mathbf{k}e_3})$, $M_{A(B)} = (C_g - \frac{1}{w^2 L_g} - \frac{i}{w R_{g,A(B)}})/C$.

For convenience, the grounding capacitance is set as $C_g = C$, $L_g = L$. As a result, in eigenfrequency ω_0 , the corresponding dissipation is $i\gamma_{A(B)} = -M_{A(B)} = -\frac{i}{R_{g,A(B)}}\sqrt{\frac{L}{C}}$. It's to be noted that $R_{g,A(B)}$ can be negative by using INIC, which corresponded to gain in the

non-Hermitian Haldane model.

Equations (9) and (E14) share the same noninteracting Hamiltonian and nearly all physical quantities are defined based on the Hamiltonian should be the same. The corresponding eigenvalue is E , and the eigenstate is $[U_{\mathbf{k},\uparrow}^A, U_{\mathbf{k},\uparrow}^B]^T$, which can be regarded as the wave function of the Haldane model with dissipation. Based on the consistency of the mathematical formula, it is straightforward to infer that we can implement the Haldane model by using designed electric circuits in Fig.8.

To realize a non-Hermitian Haldane model with uniform dissipation in bulk, the schematic of the designed electric circuit is shown in Fig.8(a). Electric circuits include circuit components such as capacitors, inductors, resistors, and negative impedance converters with current inversion (INIC). As shown in Fig.8(b), INIC can cause the current to flow in the opposite direction to the voltage, so it can be regarded as a negative resistor. In the electric circuit system, the positive (normal) resistor can correspond to dissipation (loss), and a negative resistor can correspond to gain[62].

-
- [1] C. M. Bender and S. Boettcher, Real Spectra in Non-Hermitian Hamiltonians Having PT Symmetry, *Phys. Rev. Lett.* **80**, 5243-5246 (1998).
 - [2] H. Shen, B. Zhen, and L. Fu, Topological Band Theory for Non-Hermitian Hamiltonians, *Phys. Rev. Lett.* **120**, 146402 (2018).
 - [3] T. Liu, Y. R. Zhang, Q. Ai, Z. Gong, K. Kawabata, M. Ueda, and F. Nori, Second-Order Topological Phases in Non-Hermitian Systems, *Phys. Rev. Lett.* **122**, 076801 (2019).
 - [4] X. W. Luo and C. Zhang, Higher-Order Topological Corner States Induced by Gain and Loss, *Phys. Rev. Lett.* **123**, 073601 (2019).
 - [5] N. Matsumoto, K. Kawabata, Y. Ashida, S. Furukawa, and M. Ueda, Continuous Phase Transition without Gap Closing in Non-Hermitian Quantum Many-Body Systems, *Phys. Rev. Lett.* **125**, 260601 (2020).
 - [6] F. Yang, H. Wang, M. L. Yang, C. X. Guo, X. R. Wang, G. Y. Sun, and S. P. Kou, Hidden Continuous Quantum Phase Transition without Gap Closing in Non-Hermitian Transverse Ising Model, *New J. Phys.* **24**, 043046 (2022).
 - [7] Y. Ashida, Z. Gong, and M. Ueda, Non-Hermitian Physics, *Adv. Phys.* **69**, 249 (2020).
 - [8] C. X. Guo, X. R. Wang, C. Wang, and S. P. Kou, Non-Hermitian Dynamic Strings and Anomalous Topological Degeneracy on a Non-Hermitian Toric-Code Model with Parity-Time Symmetry, *Phys. Rev. B* **101**, 144439 (2020).
 - [9] W. Wang and Z. Ma, Concurrence of Anomalous Hall Effect and Charge Density Wave in a Superconducting Topological Kagome Metal, *Phys. Rev. B* **106**, 115306 (2022).
 - [10] E. J. Bergholtz, J. C. Budich, and F. K. Kunst, Exceptional Topology of Non-Hermitian Systems, *Rev. Mod. Phys.* **93**, 015005 (2021).
 - [11] W. D. Heiss, The Physics of Exceptional Points, *J. Phys. A- Math. Theor.* **45**, 444016 (2012).
 - [12] A. Guo, G. J. Salamo, D. Duchesne, R. Morandotti, M. Volatier-Ravat, V. Aimez, G. A. Siviloglou, and D. N. Christodoulides, Observation of \mathcal{PT} -Symmetry Breaking in Complex Optical Potentials, *Phys. Rev. Lett.* **103**, 093902 (2009).
 - [13] L. Feng, Y.-L. Xu, W. S. Fegadolli, M.-H. Lu, J. E. Oliveira, V. R. Almeida, Y.-F. Chen, and A. Scherer, Experimental Demonstration of a Unidirectional Reflectionless Parity-Time Metamaterial at Optical Frequencies, *Nat. Mater.* **12**, 108 (2013).
 - [14] S. Yao, F. Song, and Z. Wang, Non-Hermitian Chern Bands, *Phys. Rev. Lett.* **121**, 136802 (2018).
 - [15] Y. Xiong, Why Does Bulk Boundary Correspondence Fail in Some Non-Hermitian Topological Models, *J. Phys. Commun.* **2**, 035043 (2018).

- [16] V. M. Martinez Alvarez, J. E. Barrios Vargas, L. E. F. Foa Torres, Non-Hermitian Robust Edge States in One Dimension: Anomalous Localization and Eigenspace Condensation at Exceptional Points, *Phys. Rev. B* **97**, 121401(R) (2018).
- [17] A. Ghatak and T. Das, New Topological Invariants in Non-Hermitian Systems, *J. Phys.: Condens. Matter* **31**, 263001 (2019).
- [18] S. Yao and Z. Wang, Edge States and Topological Invariants of Non-Hermitian Systems, *Phys. Rev. Lett.* **121**, 086803 (2018).
- [19] C. H. Lee and R. Thomale, Anatomy of Skin Modes and Topology in Non-Hermitian Systems, *Phys. Rev. B* **99**, 201103(R) (2019).
- [20] K. Yokomizo and S. Murakami, Non-Bloch Band Theory of Non-Hermitian Systems, *Phys. Rev. Lett.* **123**, 066404 (2019).
- [21] F. K. Kunst, E. Edvardsson, J. C. Budich, and E. J. Bergholtz, Biorthogonal Bulk-Boundary Correspondence in Non-Hermitian Systems, *Phys. Rev. Lett.* **121**, 026808 (2018).
- [22] C. Yin, H. Jiang, L. Li, R. Lü, and S. Chen, Geometrical Meaning of Winding Number and Its Characterization of Topological Phases in One-Dimensional Chiral Non-Hermitian Systems, *Phys. Rev. A* **97**, 052115 (2018).
- [23] K. Kawabata, K. Shiozaki, and M. Ueda, Anomalous Helical Edge States in a Non-Hermitian Chern Insulator, *Phys. Rev. B* **98**, 165148 (2018).
- [24] F. Song, S. Yao, and Z. Wang, Non-Hermitian Skin Effect and Chiral Damping in Open Quantum Systems, *Phys. Rev. Lett.* **123**, 170401 (2019).
- [25] S. Longhi, Probing Non-Hermitian Skin Effect and Non-Bloch Phase Transitions, *Phys. Rev. Res.* **1**, 023013 (2019).
- [26] K. Zhang, Z. Yang, and C. Fang, Correspondence between Winding Numbers and Skin Modes in Non-Hermitian Systems, *Phys. Rev. Lett.* **125**, 126402 (2020).
- [27] D. S. Borgnia, A. J. Kruchkov, and R. J. Slager, Non-Hermitian Boundary Modes and Topology, *Phys. Rev. Lett.* **124**, 056802 (2020).
- [28] Y. Yi and Z. Yang, Non-Hermitian Skin Modes Induced by On-Site Dissipations and Chiral Tunneling Effect, *Phys. Rev. Lett.* **125**, 186802 (2020).
- [29] N. Okuma and M. Sato, Non-Hermitian Skin Effects in Hermitian Correlated or Disordered Systems: Quantities Sensitive or Insensitive to Boundary Effects and Pseudo-Quantum-Number, *Phys. Rev. Lett.* **126**, 176601 (2021).
- [30] F. Roccati, Non-Hermitian Skin Effect as an Impurity Problem, *Phys. Rev. A* **104**, 022215 (2021).
- [31] S. Mu, C. H. Lee, L. Li, and J. Gong, Emergent Fermi Surface in a Many-Body Non-Hermitian Fermionic Chain, *Phys. Rev. B* **102**, 081115(R) (2020).
- [32] E. Lee, H. Lee, and B.J. Yang, Many-Body Approach to Non-Hermitian Physics in Fermionic Systems, *Phys. Rev. B* **101**, 121109(R) (2020).
- [33] T. Liu, J. J. He, T. Yoshida, Z. L. Xiang, and F. Nori, Non-Hermitian Topological Mott Insulators in One-Dimensional Fermionic Superlattices, *Phys. Rev. B* **102**, 235151 (2020).
- [34] D. W. Zhang, Y. L. Chen, G. Q. Zhang, L. J. Lang, Z. Li, and S. L. Zhu, Skin Superfluid, Topological Mott Insulators, and Asymmetric Dynamics in an Interacting Non-Hermitian Aubry-André-Harper Model, *Phys. Rev. B* **101**, 235150 (2020).
- [35] Z. Xu and S. Chen, Topological Bose-Mott Insulators in One-Dimensional Non-Hermitian Superlattices, *Phys. Rev. B* **102**, 035153 (2020).
- [36] K. Zhang, Z. Yang, and C. Fang, Universal Non-Hermitian Skin Effect in Two and Higher Dimensions, *Nat. Commun.* **13**, 2496 (2022).
- [37] Y. Li, C. Liang, C. Wang, C. Lu, and Y. C. Liu, Gain-Loss-Induced Hybrid Skin-Topological Effect, *Phys. Rev. Lett.* **128**, 223903 (2022).
- [38] C. H. Lee, L. Li, and J. Gong, Hybrid Higher-Order Skin Topological Modes in Non-Reciprocal Systems, *Phys. Rev. Lett.* **123**, 016805 (2019).
- [39] H. Zhang, T. Chen, L. Li, C. H. Lee, and X. Zhang, Electrical Circuit Realization of Topological Switching for the Non-Hermitian Skin Effect, *Phys. Rev. B* **107**, 085426 (2023).
- [40] K. Yokomizo and S. Murakami, Non-Bloch Bands in Two-Dimensional Non-Hermitian Systems, arXiv:2210.04412.
- [41] N. Okuma, K. Kawabata, K. Shiozaki, and M. Sato, Topological Origin of Non-Hermitian Skin Effects, *Phys. Rev. Lett.* **124**, 086801 (2020).
- [42] X. R. Wang, C. X. Guo, and S. P. Kou, Defective Edge States and Number-Anomalous Bulk-Boundary Correspondence in Non-Hermitian Topological Systems, *Phys. Rev. B* **101**, 121116(R) (2020).
- [43] X. R. Wang, C. X. Guo, Q. Du, and S. P. Kou, State-Dependent Topological Invariants and Anomalous Bulk-Boundary Correspondence in Non-Hermitian Topological Systems with Generalized Inversion Symmetry, *Chin. Phys. Lett.* **37**, 117303 (2020).
- [44] Z. Ou, Y. Wang, and L. Li, Non-Hermitian Boundary Spectral Winding, *Phys. Rev. B* **107**, L161404 (2023).
- [45] Z. Zhang, M. Rosendo López, Y. Cheng, X. Liu, and J. Christensen, Non-Hermitian Sonic Second-Order Topological Insulator, *Phys. Rev. Lett.* **122**, 195501 (2019).
- [46] E. Edvardsson, F. K. Kunst, and E. J. Bergholtz, Non-Hermitian Extensions of Higher-Order Topological Phases and Their Biorthogonal Bulk-Boundary Correspondence, *Phys. Rev. B* **99**, 081302(R) (2019).
- [47] T. Liu, Y.-R. Zhang, Q. Ai, Z. Gong, K. Kawabata, M. Ueda, and F. Nori, Second-Order Topological Phases in Non-Hermitian Systems, *Phys. Rev. Lett.* **122**, 076801 (2019).
- [48] K. Kawabata, M. Sato, and K. Shiozaki, Higher-Order Non-Hermitian Skin Effect, *Phys. Rev. B* **102**, 205118 (2020).
- [49] W. Zhu and J. Gong, Hybrid Skin-Topological Modes Without Asymmetric Couplings, *Phys. Rev. B* **106**, 035425 (2022).
- [50] D. Zou, T. Chen, W. He, J. Bao, C. H. Lee, H. Sun, and X. Zhang, Observation of Hybrid Higher-Order Skin-Topological Effect in Non-Hermitian Topoelectrical Circuits, *Nat. Commun.* **12**, 7201 (2021).
- [51] R. Lin, Tommy Tai, L. Li and C. H. Lee, Topological Non-Hermitian Skin Effect, arXiv:2302.03057.
- [52] W. Zhu and J. Gong, Photonic Corner Skin Modes, arXiv:2301.12694.
- [53] X. Zhang, Y. Tian, J.-H. Jiang, M.-H. Lu, and Y.-F. Chen, Observation of Higher-Order Non-Hermitian Skin Effect, *Nat. Commun.* **12**, 5377 (2021).
- [54] L. Li, C. H. Lee, and J. Gong, Topological Switch for Non-Hermitian Skin Effect in Cold-Atom Systems with Loss, *Phys. Rev. Lett.* **124**, 250402 (2020).
- [55] H. Zhao, X. Qiao, T. Wu, B. Midya, S. Longhi, and L. Feng, Non-Hermitian Topological Light Steering, *Science*

- 365**, 1163 (2019).
- [56] F. D. M. Haldane, Model for a Quantum Hall Effect without Landau Levels: Condensed-Matter Realization of the “Parity Anomaly”, *Phys. Rev. Lett.* **61**, 2015 (1988).
- [57] G. Jotzu, M. Messer, R. Desbuquois, M. Lebrat, T. Uehlinger, D. Greif, and T. Esslinger, Experimental Realization of the Topological Haldane Model with Ultracold Fermions, *Nature* **515**, 237 (2014).
- [58] T. E. Lee, Anomalous Edge State in a Non-Hermitian Lattice, *Phys. Rev. Lett.* **116**, 133903 (2016).
- [59] Z. Huang and D. P. Arovas, Edge States, Entanglement Spectra, and Wannier Functions in Haldane’s Honeycomb Lattice Model and its Bilayer Generalization, [arXiv:1205.6266](https://arxiv.org/abs/1205.6266).
- [60] J. Zhang, Z.-Q. Zhang, S.-G. Cheng, and H. Jiang, Topological Anderson Insulator via Disorder-Recovered Average Symmetry, *Phys. Rev. B* **106**, 195304 (2022).
- [61] Y. Yang, D. Zhu, Z. Hang, and Y. Chong, Observation of antichiral edge states in a circuit lattice, *Sci. China Phys. Mech. Astron.* **64**, 257011 (2021).
- [62] S. Liu, S. Ma, C. Yang, L. Zhang, W. Gao, J. Yuan, J. Tie, and S. Zhang, Gain- and Loss-Induced Topological Insulating Phase in a Non-Hermitian Electrical Circuit, *Phys. Rev. Appl.* **13**, 014047 (2020).

Properties	Traditional NHSE	Non-Hermitian chiral skin effect
Boundary condition	Open boundary condition	Period boundary condition
Normal/ Anomalous	Normal	Anomalous: Cannot be observed in a one-dimensional model
Localized position	All eigenstates are localized at the system boundary	Chiral edge states are localized at the global dissipative domain walls
Topological Invariant / “order parameter” for NHSE	Winding number in complex energy space	Global dissipation: the effect of subtracting the average dissipation from the spatial distribution of dissipation
Energy spectrum structure	Form a closed loop	Chiral states form a straight line with fixed imaginary part in complex energy space